

3D structural and atomic-scale analysis of lath martensite: Effect of the transformation sequence



L. Morsdorf, C.C. Tasan^{*}, D. Ponge, D. Raabe

Max-Planck-Institut für Eisenforschung, Max-Planck-Straße 1, 40237 Düsseldorf, Germany

ARTICLE INFO

Article history:

Received 22 December 2014

Revised 4 May 2015

Accepted 13 May 2015

Keywords:

Lath martensite
3D

Atom probe tomography
ECCI
EBSD

ABSTRACT

To improve the fundamental understanding of the multi-scale characteristics of martensitic microstructures and their micro-mechanical properties, a multi-probe methodology is developed and applied to low-carbon lath martensitic model alloys. The approach is based on the joint employment of electron channeling contrast imaging (ECCI), electron backscatter diffraction (EBSD), transmission electron microscopy (TEM), atom probe tomography (APT) and nanoindentation, in conjunction with high precision and large field-of-view 3D serial sectioning. This methodology enabled us to resolve (i) size variations of martensite sub-units, (ii) associated dislocation sub-structures, (iii) chemical heterogeneities, and (iv) the resulting local mechanical properties. The identified interrelated microstructure heterogeneity is discussed and related to the martensitic transformation sequence, which is proposed to intrinsically lead to formation of a nano-composite structure in low-carbon martensitic steels.

© 2015 Acta Materialia Inc. Published by Elsevier Ltd. All rights reserved.

1. Introduction

This report aims at providing an improved fundamental understanding on the micro-mechanical response of lath martensitic microstructures. Lath martensite is of immense importance for structural alloys, since it is among the major strength-providing microstructural constituents in martensitic or multi-phase steels (e.g. dual phase steel, transformation-induced plasticity steel, complex phase steels, quench-partition steels, etc.). Despite its long history and use, efforts to better understand the microstructure development and the mechanical behavior of lath martensite are still ongoing. Here, we are specifically interested in martensitic constituent size variation effects which have been rarely investigated so far [1–3], but drastically influence e.g. the autotempering behavior [4] and toughness properties [5]. Effectively any analysis associated with lath martensitic microstructures is hindered due to the complexities arising from (i) crystallographic and (ii) compositional aspects of the underlying microstructure. In order to motivate the novel analysis strategy developed here, we first discuss these two challenges in the following two paragraphs.

Regarding martensite crystallography most pioneering works were based on transmission electron microscopy analyses [6,7]. TEM provides sufficient spatial resolution to resolve fine martensitic features (e.g. laths [6]), however, it provides only limited statistics of larger martensitic constituents (e.g. prior austenite

grains) due to its limited field of view arising from the specimen and beam geometries. It is the development of the electron backscatter diffraction (EBSD) technique that enabled the systematic characterization of the hierarchical martensitic microstructure spanning multiple scales, i.e. ranging from prior austenite grains of hundreds of microns down to laths of tens of nanometers [8–11]. Yet, it is also clear that the standard 2D EBSD-based analysis provides a rather simplified representation of the lath martensite crystallography. For example, 3D EBSD and 3D FIB [12–15] analyses, as well as TEM observations [1,16,17] reveal significant heterogeneities in the size and morphology of martensite sub-units even within a single alloy, which cannot be fully captured by stand-alone 2D investigations. Also, even in optimized conditions, EBSD cannot resolve the fine details of the martensitic sub-structure.

Regarding martensite composition, similar progress was made due to the advances in another ‘enabling’ technique, namely, atom probe tomography (APT) [18–22]. Similar to EBSD providing wider access to martensite crystallography, APT triggered investigations of e.g. carbon (C) Cottrell atmospheres and segregation [23–29], precipitation reactions in martensite [30–32] and austenite layers in martensite [33,34]. Arguably the most critical among these is the analysis of C in martensite, since interstitial C plays one of the major roles in the properties of martensite [35–38]. A large number of recent APT based reports provide evidence of significant C distribution heterogeneity in martensite, which is taking place at a scale that was not accessible with conventional techniques (EDX,

^{*} Corresponding author.

WDX, EELS, etc.). However, though only rarely commented on in the literature, this type of C variation does not occur homogeneously throughout a given martensitic microstructure [23,39], hence, probing a sufficiently representative volume by APT is an issue. Further, APT has its own limitations, as in most cases it requires direct coupling to a diffraction based technique to identify the crystallographic nature of segregation zones [40,41]. Without correlative techniques helping to interpret APT data, analyses often include speculation on the origin of such chemical heterogeneities. One example is e.g. C enrichment in thin film austenite which is hard to distinguish from C segregation to lath boundaries with chemical mapping data only, i.e. without the aid from electron diffraction [33,39].

The complexity arising from the crystallographic and compositional heterogeneities inevitably affects the mechanical response of the material [42]. Recent micro-testing efforts successfully identified indications of these differences, e.g. by micro-tension [43] and micro-compression [44]. An elegant example is the discussion of the effectiveness of block vs. sub-block boundaries against slip transition through focused ion beam milled micro-beam bending experiments [45]. However, the hierarchy and the extreme fineness of the martensite microstructure require manufacturing of even smaller (sub-micron) sized samples for systematic investigations, imposing substantial experimental challenges due to FIB-induced damage, influence of geometric imperfections in micro-specimens, and alignment issues.

These rather fundamental challenges require a dedicated coupled approach that can ‘simultaneously’ (i) probe statistically-representative areas of coarser martensitic constituents (e.g. blocks, packets, prior austenite grains, etc.) in 3D, (ii) resolve fine martensitic constituents (laths, lath boundaries, dislocation densities, twins, etc.) in 3D, and couple these analyses to (iii) atomic resolution compositional mapping and (iv) high-resolution mechanical mapping. Such an approach enables unraveling of various aspects of martensite behavior, e.g. its 3D morphology, autotempering effects and strengthening contributions of the individual defects. The methodology presented here satisfies these requirements. The approach is based on electron channeling contrast imaging (ECCI), which successfully bridges the scale gap between EBSD and TEM in terms of resolution as well as field of view imaging [46,47]. We show that high resolution ECCI resolves smallest martensite sub-units and its internal defect structures such as dislocation networks and twins at a wide field of view [48–50]. Moreover, we demonstrate that it enables a direct coupling to diffraction information (by EBSD or TEM), 3D morphology (by serial sectioning) and chemistry (by APT) as well as local mechanical properties (by nanoindentation). Nanoindentation avoids the majority of the challenges mentioned above for FIB-based micro-testing approaches, and provides higher spatial resolution to probe the fine crystallographic and compositional heterogeneities mentioned above [51,52]. However, so far it was not related to size variations in lath martensite μ -constituents.

2. Experimental

The here developed multi-probe characterization approach was applied on a Fe–0.13C–5.1Ni–<0.002S–<0.002P model (wt.%) alloy, although several other martensitic steels were also characterized for partial comparisons. The Fe–C–Ni alloys, non-commercial grades provided by ArcelorMittal Research Center in Maizières, France, were austenitized at 900 °C for 5 min and subsequently quenched in water to obtain a fully martensitic microstructure. The experimental steps are schematically shown in Fig. 1.

The first step in our methodology is a large field-of-view EBSD measurement (Fig. 1). Then, four micro-indents (HV1) were made for depth-calibration during serial sectioning. We employ

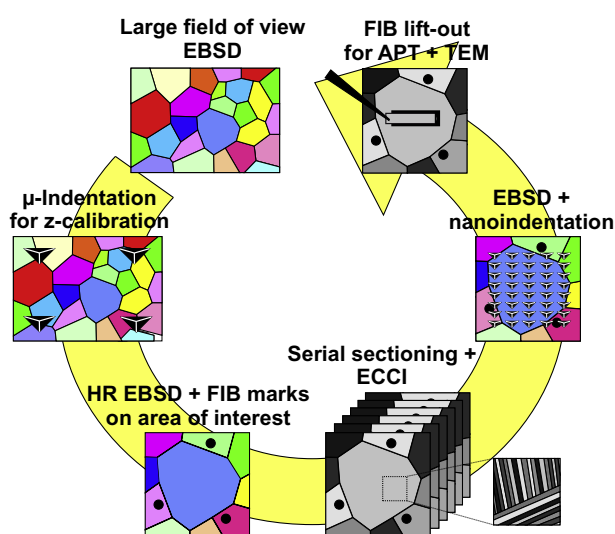


Fig. 1. The employed 3D multi-probe characterization approach that involves depth-resolved serial sectioning, ECCI, EBSD, nanoindentation, APT and TEM analyses. Nanoindents are significantly exaggerated for visual clarity.

depth-resolved colloidal silica chemo-mechanical polishing for sectional material removal. Compared to most other FIB-based serial sectioning approaches, the colloidal silica polishing approach provides larger field-of-view and avoids ion-beam knock-on damage [53]. The latter is especially critical for ECCI [46]. To inhibit image stacking errors, three surface-perpendicular fiducial holes were FIB-milled at the first step in the periphery of the area of interest. A HELIOS Nanolab 600i dual beam microscope was used for FIB milling. For each sectioning step the sample was subjected to a machine-controlled polishing routine. The spacing between each section was controlled through the change in the length of the diagonals of the indents made before polishing. For the data that will be presented next, after one calibration step of $\sim 1.5 \mu\text{m}$, the z-removal was kept constant to steps of $\sim 500 \text{ nm}$. The serial sectioning was stopped after the collection of a 3D stack of eight sections and a total z-removal of $\sim 4 \mu\text{m}$, since sufficient data were collected. At each section, a chosen prior austenite grain was characterized by ECCI and when necessary by EBSD. ECCI and EBSD measurements with 30–50 nm step size were carried out using a Zeiss “Merlin” FEG-SEM operated at 30 kV and a Jeol JSM-6500F FEG-SEM operated at 15 kV, respectively. The EBSD data were used to reconstruct the prior austenite grains by means of a reconstruction software that functions based on the orientation relationship between austenite and martensite [54]. The investigated “prior austenite grain” was then subjected to a fine grid of nanoindents on the as-polished surface using a Hysitron TriboScope 900. A Berkovich indenter geometry was used for indentation with a constant force of 300 μN to create a $2 \mu\text{m} \times 2 \mu\text{m}$ cell pattern of 209 indents in total. Additional ECCI and EBSD characterization of the indented grain allows for full coupling of the nanohardness distribution to the lath martensite hierarchical substructure.

These analyses enable well-informed sample location specification for extracting secondary specimens for atom probe tomography as well as for transmission electron microscopy. These samples were prepared through a site-specific FIB lift-out technique. The former was carried out using a Local Electrode Atom Probe (LEAP™ 3000X HR, CAMECA Instruments) maintained under ultrahigh vacuum conditions ($\sim 10^{-11}$ Torr) and operated in voltage and laser mode. The pulse fraction and pulse repetition rate were 15% and 200 kHz in the voltage mode, respectively. In laser mode, the laser energy was 0.4 nJ and the pulse repetition rate was 250 kHz. The tip temperature was maintained at 60 K. The

acquired data has been analyzed using the IVAS™ software (CAMECA Inc.). The ranging of mass spectra especially regarding C peaks was carried out according to [55]. Regarding the TEM-lamella samples, bright-field TEM imaging was carried out using a Philips CM 20 TEM operated at 200 kV. Nanodiffraction mapping (ASTAR) with a step size of 2 nm was conducted by means of a Jeol JEM-2200FS TEM operated at 200 kV.

3. Results

The results are presented here mainly following the methodological sequence shown in Fig. 1 (except for the APT results preceding nanoindentation results) under three sub-sections, namely, *Heterogeneity in morphology and defect density*; *Heterogeneity in local chemical composition*; and (the resulting) *Heterogeneity in mechanical response*.

3.1. Heterogeneity in morphology and defect density

We start our multi-probe analysis of the lath martensitic microstructure of the Fe–0.15C–5Ni (wt.%) alloy with the large field of view EBSD measurement (Fig. 2a). Here an overlay of the prior austenite grain boundary map on the kernel average misorientation (KAM) map is shown. Rather than a typical crystal orientation map (e.g. an inverse pole figure map), the KAM map is deliberately chosen here as the starting point since it reveals a striking feature: most prior austenite grains have large low-KAM regions (some indicated by arrows) clearly separated from the matrix lath martensite, characterized by its higher KAM values. Such low KAM regions of various sizes are frequently found across the entire microstructure. To zoom further in, Fig. 2b₁ shows an inverse pole figure (IPF) map of the interior of one prior austenite grain with ~25 µm grain size embedded in the reconstructed prior austenite grain structure. Fig. 2b₂ shows an electron channeling contrast image of the same prior austenite grain revealing the martensite structure in terms of sharp changes in diffraction contrast. The ECCI map reveals that this prior austenite grain is mainly composed of blocks of conventional thin laths (see arrow “d₂”). The average lath thickness is ~200 nm including thin laths ranging from ~50 nm to ~500 nm in thickness. ECCI also confirms the presence of boundary-free regions corresponding to the low KAM regions in Fig. 2a₁, some of which exceed the typical lath dimensions by about an order of magnitude in thickness direction (see arrow “d₁”).

Examples for a relatively larger boundary-free region and for a conventional lath region are shown at higher magnification by means of EBSD and ECCI in Fig. 2c₁–c₂ and Fig. 2d₁–d₂, respectively. Within the marked region in c₁, the IPF map shows a homogeneous lattice orientation. Correspondingly, boundaries indicated by sharp contrast changes are absent in ECCI of the same region (c₂). The channeling contrast is instead gradually changing throughout this boundary-free region indicating gradual lattice rotation. The dimensions obtained from the 2D observation yield a maximum thickness of ~3.5 µm and a length of ~15 µm. Due to the absence of any internal interfaces these large regions are in the following considered as ‘coarse laths’, since laths are conventionally considered as the smallest sub-unit of the well-known martensite hierarchy [8]. Note however that coarse laths do not always have the same size (Fig. 2b₂). Similar features were observed by Fonda et al. introducing those regions as coarse martensite [1].

Fig. 2d₁ shows an IPF map of a region containing martensite sub-units of the other extreme, i.e. the conventional laths. In Fig. 2d₂ the interfaces identified by EBSD are overlaid to ECCI. Note that only a small portion of the boundaries revealed by ECCI is also resolved by EBSD. These observations underline the

limitation of EBSD in resolving some of the individual thin laths, which are misoriented by only 1° to 5°, due to limited spatial and angular resolution. Instead, ECCI of the same region clearly reveals both, lath boundaries and intra-lath substructures. In fact, it is this capability of ECCI that enables the observation of strong size variations in laths at a wide field of view.

At first view, the 2D image (Fig. 2c₂) might suggest that the coarse laths are simply conventional laths that lay parallel to the surface. The ‘real’ 3D shape cannot be accessed by only 2D imaging though. In order to assess the sub-surface extension of the coarse laths, the 3D serial sectioning methodology described in Fig. 1 is applied. The evolution of this prior austenite grain along the z-direction is investigated by 3D serial sectioning coupled to ECCI. Three coarse laths (see red outlines in Fig. 3a) were especially tracked at every section. Their propagation in z-direction is illustrated in Fig. 3a. The analysis reveals that these three coarse laths all extend throughout the entire z-range of 4 µm. Apparently, their z-extension (>4 µm for each) even exceeds the maximum 2D thickness measured from the surface observation (~3.5 µm, ~3.4 µm, ~1.6 µm). Regarding the morphology, the 3D analysis reveals that the coarse laths develop in a wedge shape. For a final confirmation, Fig. 3b shows a 3D cube montage of a coarse lath region. The sample surface is observed with ECCI in SEM environment and the cross-sectional view is obtained from a FIB-lamella lifted-out from the very same position and analyzed by TEM bright-field imaging. For better clarity the border lines of the coarse lath are marked in both images. Again the significant size difference becomes evident regarding the coarse lath being embedded in a matrix of conventional thin laths on both sides.

In summary, the investigated lath martensitic microstructure contains a surprisingly broad variety of lath sizes. In the following, for the sake of clear explanation of the complex processes involved, laths with thicknesses ranging from ~50 nm to ~500 nm are referred to as conventional thin laths and laths that e.g. extend up to ~3.5 µm in the thickness direction are referred to as coarse laths. As the lath thickness increases, the lath lengths typically also increase (i.e. the long direction of coarser laths often exceeds the typical length of thin laths) however, this is more difficult to accurately quantify even with the 3D approach presented here. Instead, the overall area fraction of coarse laths is determined by image analysis based on three individual KAM maps from EBSD measurements (i.e. Fig. 2a). Low KAM regions with a minimum size of 5 µm² are considered as coarse laths resulting in an area fraction of $8.8 \pm 0.6\%$. Note also that both, coarse and thin laths are usually maintained throughout the entire sectioning distance proving a depth dimension of at least 4 µm. The latter will be demonstrated in Fig. 4d, where the defect structure of a single thin lath is analyzed through-out the depth direction.

To better understand the internal lath substructures, results of high resolution ECCI are presented in Fig. 4 for both, coarse (a₁) and thin (b) lath regions. The entire coarse lath region is in channeling condition (dark) as it is indicated by homogeneous bcc lattice orientation shown from EBSD (a₂). The defect structure is then revealed by ECCI in terms of deviations from the ‘perfect’ channeling condition. Lattice defects therefore appear brighter than the lattice itself creating the dark background [46]. For better visibility of the defect structure, ECCI images are inverted in the following, so that the defect structures appear dark on a bright background.

Fig. 4a₁ reveals that dislocation cell networks spread over the entire coarse lath region. The topography optimized SE image of exactly the same region confirms that the surface is flat and featureless, except for the presence of some silicon oxide particles from polishing (Fig. 4a₃). A value for the dislocation density is estimated following [56] and yields $1.46 \pm 0.03 \times 10^{14} \text{ m}^{-2}$. Dislocation networks are also observed in some of the thin laths (Fig. 4b) with slightly higher dislocation densities of $1.62 \pm 0.16 \times 10^{14} \text{ m}^{-2}$. The

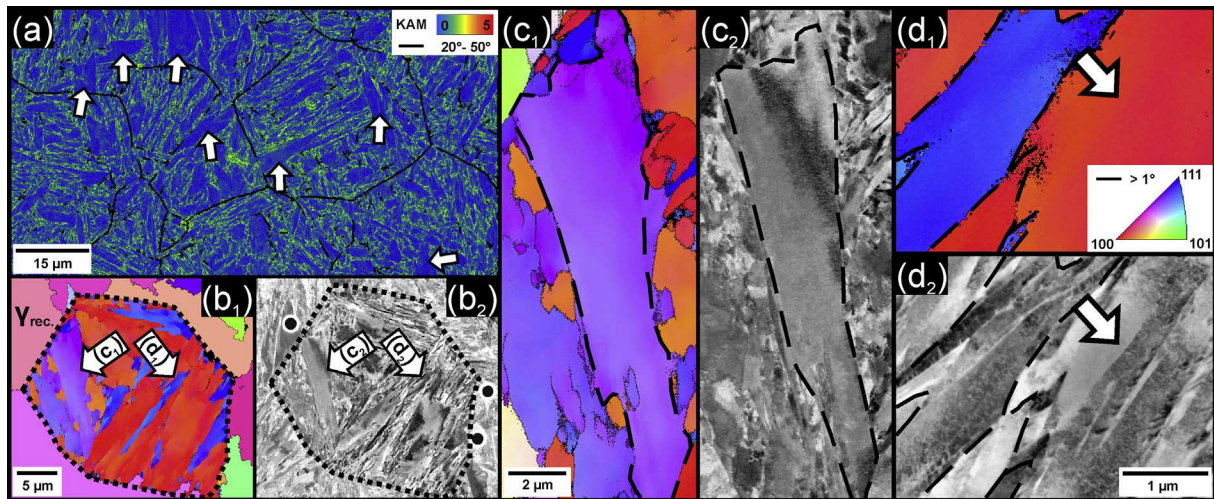


Fig. 2. EBSD vs. ECCI characterization of lath martensite in a Fe-0.13C-5.1Ni (wt.%) model alloy, focusing on one prior austenite grain; (a) overview KAM map with prior austenite boundary overlay, showing extended low and high KAM regions; (b₁) IPF map showing lath martensite in one prior austenite grain from the reconstructed prior austenite structure; (b₂) ECCI showing the same prior austenite grain as in (b₁). Higher magnification ECCI analyses reveal extended boundary-free regions (c₂) and conventional thin lath regions (d₂). (c₁) and (d₁) present IPF maps of the respective regions obtained by EBSD, however with lower spatial resolution compared to ECCI. Conventional lath boundaries are observed clearly by ECCI, but not always with EBSD (see the white arrows in d₁ and d₂).

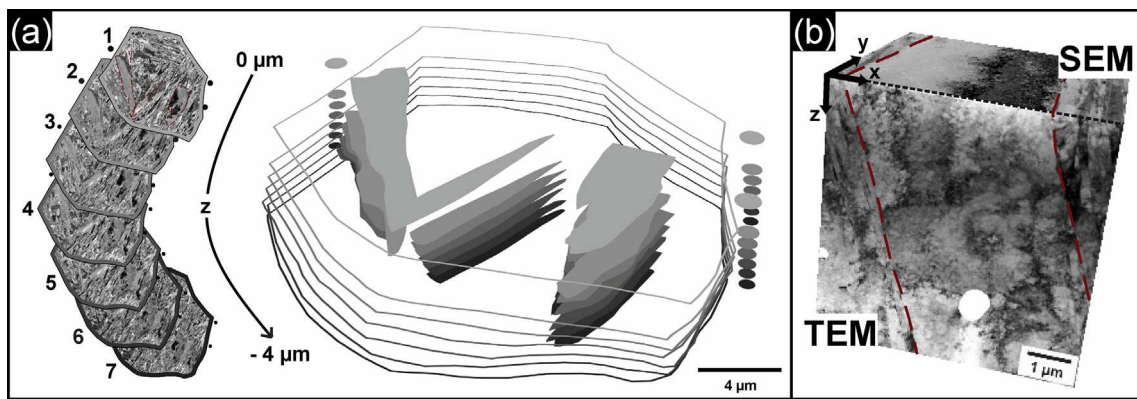


Fig. 3. (a) 3D characterization of the prior austenite grain introduced in Fig. 2. The outlines of the coarse laths, prior austenite grain and calibrating FIB-milled holes are shown as they are obtained from the raw ECCI image series on the left. The presence of coarse laths in the microstructure is proven by both, serial sectioning (a) and correlative SEM and TEM analyses (b). In (b) ECCI is spatially coupled to BF TEM imaging, both showing a coarse lath region.

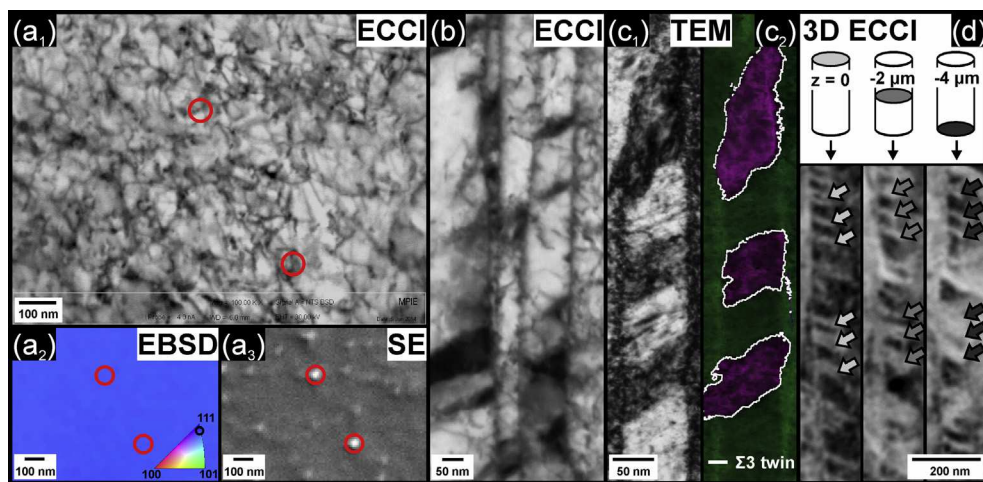


Fig. 4. Internal defect structures in coarse (a) and thin laths (b–d); (a₁) ECCI (inverted for visual clarity) of a coarse lath with corresponding lattice orientation revealed by IPF map from EBSD measurement (a₂) and topography revealed by low-kV SE (a₃); ECCI (inverted for visual clarity) of thin laths (b), bright-field TEM (c₁) and corresponding ASTAR characterization (c₂) shown as IPF map overlaid with grayscale image quality; (d) depth-evolution of twinned thin laths as obtained from 3D serial sectioning.

evaluation of dislocation structures by ECCI is also confirmed by BF TEM analyses on the coarse lath region presented in Fig. 3b showing structurally similar dislocation networks in agreement with the ECCI surface observations of the very same region.

Apart from dislocations, plate-like defects are frequently observed in thin laths. These defects were also found by bright-field TEM imaging of the TEM lamella, shown in Fig. 4c₁, and are crystallographically characterized by nanodiffraction as shown in Fig. 4c₂. The orientation map reveals $\Sigma 3$ twin grain boundaries between the plate-like defects and the surrounding thin laths indicating internally twinned laths present in the microstructure. 3D serial sectioning reveals that those twins also propagate in z-direction confirming a plate-like morphology (Fig. 4d).

3.2. Heterogeneity in local chemical composition

Local composition fluctuations within the lath martensitic microstructure are studied by means of APT and with respect to the observed lath size distribution. In the following only the distribution of C atoms will be described owing to the homogeneous distribution of iron and nickel in all measurements. Fig. 5a₁–a₃ shows the lift-out region for the APT measurements initially characterized by SE (a₁), ECCI (a₂) and EBSD (a₃). A coarse lath region connected to a prior austenite grain boundary, similar to the aforementioned examples, is marked and protected from ion beam damage by a strip of Pt, and finally lifted-out. During tip sharpening the Pt layer is removed in the final stages of the preparation to ensure that the investigated volume originates from just below the sample surface and therefore can be correlated to the 2D surface characterization.

Fig. 5b₁ and 5c shows two reconstructed tip volumes in terms of the corresponding C atom maps and 3 at.% C iso-concentration surfaces. The red marked sample (Fig. 5b₁) originates from the very edge of the lift-out region and therefore contains the thin edge of the targeted coarse lath adjacent to thinner laths. The blue marked sample (Fig. 5c) originates from the lift-out center ensuring the tip volume coming from the coarse lath (as illustrated in Fig. 5a₁). In the former, starting with the C atom map presented in Fig. 5b₁, three regions can be identified (I, II, III). These are well-separated by planar interfaces enriched in C (which thus both morphologically and compositionally resemble lath boundaries). We identify in reasonable certainty that the middle region (II) is a thin lath with a thickness of ~ 60 nm, since it is completely enclosed by two such decorated interfaces. This is also in agreement with the fact that the investigated tip volume is chosen from the very edge of the lift-out region and therefore it is likely to contain thin laths as well. The C enrichment at the lath boundary separating the middle lath (II) from the lower lath (III) is evaluated by 1D concentration profile analysis and yields ~ 2.3 at.% C enrichment (Fig. 5e) which is in good agreement with previous studies on low-C lath martensite [23,26,28].

Apart from its presence at the lath boundary, C is strongly segregated to 1D features in the lath interior (which follow the morphology of single dislocations shown in Fig. 4a₁ by ECCI) as highlighted in Fig. 5b₁ and d₁. The C excess is obtained from proximity analysis of the marked C iso-concentration surface, as presented in Fig. 5d₃, and reaches a maximum value of ~ 8.0 at.% which agrees well to previous studies on C Cottrell atmospheres in bcc Fe [27,29]. Fig. 5b₂ shows a series of C iso-concentration surfaces ranging from 1 at.% to 4 at.%. Starting with the latter, the highest C enrichment is observed at dislocations in the middle lath region. The 3 at.% C and 2 at.% C iso-concentration surfaces additionally indicate the two lath boundaries in terms of the segregation of C. The 1 at.% and 2 at.% C iso-concentration surfaces reveal that C is significantly stronger segregated in the middle lath (II) compared to the lower lath (III) (Fig. 5b₂). The same striking

result is obtained from the 1D concentration profile across the lath boundary (Fig. 5e) yielding matrix values of ~ 0.3 at.% C in the middle lath compared to ~ 0.7 at.% C in the lower lath, which is roughly the nominal C concentration of the alloy.

The second reconstructed tip volume from the coarse lath interior is presented in Fig. 5c in terms of a C atom map with 3 at.% C iso-concentration surfaces. The matrix C is again obtained from 1D concentration profile analysis yielding almost constantly ~ 0.15 at.% C (Fig. 5e). This value is in good agreement with the other APT measurements from the coarse lath interior carried out in voltage mode (not presented here) and with previous studies [23,26,28]. A few extended zones of strong C enrichment can be identified in the reconstructed tip volume. Strikingly, their morphologies are distinctly different compared to the thin lath which is illustrated by the comparison of two iso-concentration surfaces in Fig. 5d_{1–2}. In the coarse lath interior C is segregated in plate-like shapes (Fig. 5d₂) with maximum C concentrations of ~ 9.2 at.%. The same morphologies of regions with such C segregations have been also found in the other APT measurements conducted on coarse lath interiors. This quantitative analysis reveals that the extent of C segregation is more progressed in the coarse lath (i.e. the matrix has up to 4–5 times lower matrix C content) compared to the analyzed thin laths.

3.3. Heterogeneity in local mechanical response

The micro-mechanical consequences of the observed heterogeneity in lath sizes, defect sub-structures and compositions are investigated by nanoindentation tests carried out on the same prior austenite grain that was subjected to 3D analysis (shown in Fig. 3). Fig. 6a shows a color coded nanohardness map overlaid to an ECCI overview image of the complete region and the corresponding IPF map from the EBSD analysis is shown in Fig. 6b. The widespread of colors seen in the overlay represents a nanohardness range between 4.6 and 9.7 GPa, which at first glance seems to indicate random fluctuations due to experimental scatter. In fact, it is clear even prior to this observation that the nanoindentation analysis of the extremely fine lath martensite microstructure is challenging. However, this technique is the highest resolution mechanical probing method available, and the majority of the expected experimental uncertainty in nanoindentation analysis of lath martensite is due to random errors arising from limited statistics.¹ In order to increase precision (i.e. decrease random errors), special attention was paid (i) to decrease the interaction volume of nanoindentation measurements by lowering the indentation load to 300 μ N, and (ii) to group the results from the nanoindents into four categories using corresponding EBSD and ECCI data in a comparative manner (Fig. 6d):

- Coarse lath bulk ($H_{\text{Coarse_Bulk}}$), i.e. away from boundaries as in Fig. 6c₁,²: mean of 21 indents.
- Thin lath bulk ($H_{\text{Thin_Bulk}}$): mean of 13 indents.
- Coarse lath near boundary ($H_{\text{Coarse_Boundary}}$) as in Fig. 6c₂: mean of 18 indents.
- Thin lath near boundary ($H_{\text{Thin_Boundary}}$): mean of 130 indents.

This classification, which is schematically shown as insets in Fig. 6e, decreases the apparent scatter in hardness values as intended (see the error bars in Fig. 6e), and moreover, enables quantification of sole effects of different factors influencing the

¹ Here we assume that the intrinsic size effects do not differ between thin and coarse laths, and hence, cause no systematic errors in the obtained hardness values.

² Indents are categorized as not strongly affected by boundaries when no boundary ($> 1^\circ$ misorientation from EBSD analysis) is present within the plastic zone around the indent.

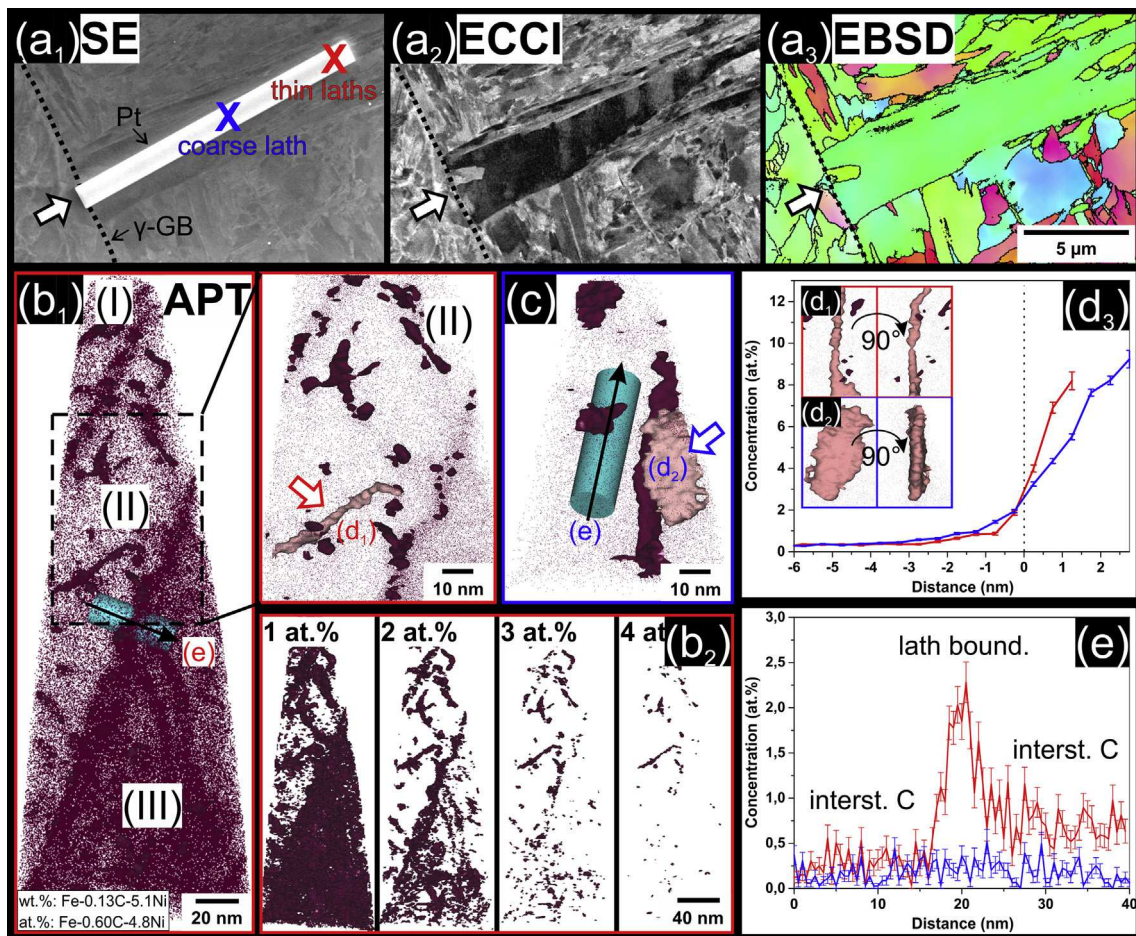


Fig. 5. Pre-APT characterization of coarse lath target lift-out region by SE imaging (a₁), ECCI (a₂) and EBSD (a₃); reconstructed tip volumes with C atom maps containing 3 at.% C iso-concentration surfaces for fine laths (b₁ 'red') and coarse lath interior (c 'blue'); (b₂) series of iso-concentration surfaces of the reconstructed tip volume in (b₁); (d₁₋₂) comparison of iso-concentration surface morphologies and corresponding proximity analysis of C concentration with 0.5 nm bin size (d₃); (e) 1D concentration profile analyses of C concentration along the cylinders shown in (b₁) and (c) with 0.5 nm bin size. 3D animations of the APT measurements are available online for the thin laths (Fig. A1) and the coarse lath (Fig. A2). (For interpretation of the references to color in this figure legend, the reader is referred to the web version of this article.)

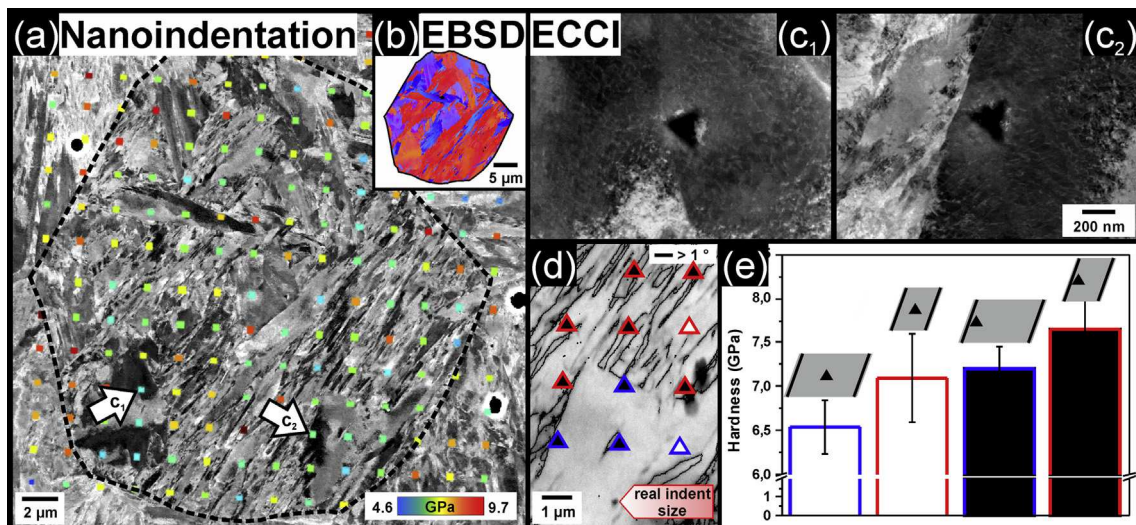


Fig. 6. (a) Nanoindentation map on prior austenite grain subjected before to 3D microstructure characterization (IPF map from EBSD analysis in (b)). Indents either probe the lath interior (c₁) or contain boundary effects (c₂) and are grouped accordingly as evaluated from EBSD boundary analysis (d). Note that in (d) the indent marker is vastly exaggerated in size for visual clarity; (e) averaged nanohardness of coarse and thin laths combined with the effect of boundaries accounting for the fine-scale indent-microstructure interaction.

nanohardness: e.g. lath size, boundaries, etc. The averaged nanohardness values are obtained from at least 13 individual indents in each group.

Three main results can be extracted from the results shown in Fig. 6e. First, the average nanohardness of coarse laths is ~ 0.7 GPa higher near a boundary compared to the bulk (i.e. $H_{\text{Coarse_Bulk}} < H_{\text{Coarse_Boundary}}$). Almost the same boundary effect is observed for the thinner laths, that is, $H_{\text{Thin_Bulk}}$ is again ~ 0.6 GPa lower than $H_{\text{Thin_Boundary}}$, suggesting that the nanoin-dents on the bulk of the thinner laths are not strongly affected by the nearby boundary. This allows us to quantitatively compare the bulk hardness of the coarse and thin laths, without any influence of the boundaries. The comparison reveals the interesting result that coarse laths ($H_{\text{Coarse_Bulk}} = 6.5$ GPa) are softer than the thinner ones ($H_{\text{Thin_Bulk}} = 7.1$ GPa). This is true even when the boundary effects are included: the average nanohardness of coarse laths is again lower than of thin laths by ~ 0.4 GPa (i.e. $H_{\text{Coarse_Boundary}} < H_{\text{Thin_Boundary}}$).

4. Discussion

4.1. Origin of lath size heterogeneity

The 3D ECCI microstructure characterization clearly shows that the investigated lath martensitic microstructure contains coarse laths ($> 1.5 \mu\text{m}$ in thickness) that significantly exceed the dimensions of conventional thin laths ($50\text{--}500 \text{ nm}$ in thickness) (see Fig. 3). Those internally boundary-free regions are frequently found within the microstructure and are often connected to prior austenite grain boundaries. In terms of defect substructures therein, ECCI revealed wide dislocation cell networks in the coarse laths with slightly lower dislocation densities compared to the thin laths.

Similar size distributions were reported in lower bainite and also recently in martensite, and the occurrence of extended boundary-free regions was proposed to develop through a coalescence mechanism [57,58]. It is argued that adjacent parallel laths with almost equal orientations are first separated by low-angle boundaries right after their nucleation, but with on-going transformation a coalesced plate, which extends in the thickness direction, is energetically favored. Two necessary conditions for the coalescence process are formulated. First, the initial growth of laths should not be hindered by a microstructural constituent, which is fulfilled for the earliest forming laths growing into the untransformed “soft” austenite. Second, the higher strain energy associated with the coalesced plate must be compensated by an adequate driving force, which is fulfilled for large undercooling below B_s , e.g. during isothermal transformation right above M_s [59].

Only few indications of the coalescence process are observed in the 3D ECCI analysis presented here, e.g. few coarse laths gradually split up to thin laths separated by lath boundaries as it was proposed in [57], but the TEM analysis did not reveal former boundaries in the coarse lath region (as reported in [57]). This motivated us to consider the differences between the bainitic and martensitic transformations in the further discussion: In case of the martensitic transformation, the start of the phase transformation is shifted to lower temperatures compared to a bainitic transformation, and limited to a narrow time window due to quenching. Thus, close to M_f , where the gain in free energy is highest, the available thermal energy is limited, and the time restricted. Considering the microstructural rearrangements associated with the proposed coalescence mechanism (movement of dislocations, dissolution of thin film austenite and obligatory C diffusion and precipitation), the second condition proposed above is more difficult to fulfill for martensitic transformations. Moreover, the characteristic wedge-shape morphology of the coarse laths reported here (and also elsewhere [4,14]) is linked to the growth of

martensite laths [3], however, is not yet directly linked to the coalescence mechanism.

Another point of view for the development of the coarse lath structures could be based on the evolution of the untransformed austenite through the process of the martensitic transformation. As pointed out by Miyamoto et al., the transformation strain is plastically accommodated by the surrounding austenite, and hence its state plays a major role in determining the transformed volume [60]. Fig. 7 illustrates this effect schematically step-by-step through the course of the martensitic transformation from M_s to M_f . Right above the M_s temperature the austenite is soft and has a low defect density, causing the smallest resistance against a growing martensitic lath. However, from the formation of the first martensite laths onwards during cooling, the retained austenite is progressively hardened by (i) reduced temperature and (ii) increasing density of accommodation dislocations due to shape deformation involved in the (previous) martensitic transformation. As the transformation proceeds, this decrease in compliance causes an increasing resistance to the progressing martensitic transformation (i.e. to the growth of the next lath to form), especially in the direct vicinity of a recently-transformed lath. The mechanical stabilization of austenite during transformation was also observed by van Bohemen and Sietsma, who studied the martensitic transformation after partial transformation of austenite to bainite by dilatometry [61]. When the coarse laths have formed, the progressing nucleation of laths might be auto-catalytically triggered by the high defect density in the austenite surrounding the freshly formed martensite, so that a high number of thin laths can nucleate e.g. from the introduced martensite-austenite interface. In this regard, coarse and thin laths might be also distinguished according to their formation mechanisms. Close to M_f , the small fraction of the remaining untransformed austenite is highly constrained and thus highly stable [62,63]. In fact, we attribute the internal twinning of some of the thin martensite laths (see Fig. 3) to the presence of this constraint that apparently requires the activation of another plastic strain accommodation mechanism as illustrated in Fig. 7.³ In the meantime, the early formed martensite is autotempered during quenching and softened due to C segregation processes (indicated in Fig. 7a) which is further discussed in the next sub-section.

There are three confirming observations to the proposed process: (i) We often observe that the flat end of the coarse laths is directly connected to a prior austenite grain boundary (see Figs. 2, 3, 5 and 9), i.e. a typical initiation site for martensitic phase transformations [66]. This can be regarded as a strong indication that the coarse laths do indeed form earliest in the martensitic transformation sequence. (ii) The dislocations in the continuously strengthened austenite are inherited to the transforming martensite [5,57] in addition to the dislocations in martensite that were introduced due to the transformation strain. The latter is assumed to be almost independent from the transformation sequence. In total, the slightly lower defect density in the ECCI observations of coarse laths (Fig. 4) confirms that they transform early in the sequence into “soft” austenite. (iii) We carried out a comparative analysis on two other alloys, the high temperature microstructures of which are shown schematically in Fig. 7b. The amount of coarse laths in the investigated Fe–0.13C–5.1Ni alloy (shown in the middle of the graph) is compared to an alloy with higher C content of 0.3 wt. % (shown on the right side) and an alloy with smaller prior austenite grain size obtained after 50°C lower austenitization treatment (shown on the left side). We observe a clear trend that shows that the corresponding coarse lath area fractions are lower in both cases (4.7 area.% for finer austenite grain size and 3.9 area.%

³ Note that internally twinned lath martensite has been reported in the literature before [36,64], although not linked to lath size variations. In plate martensite twinning occurs regularly [65].

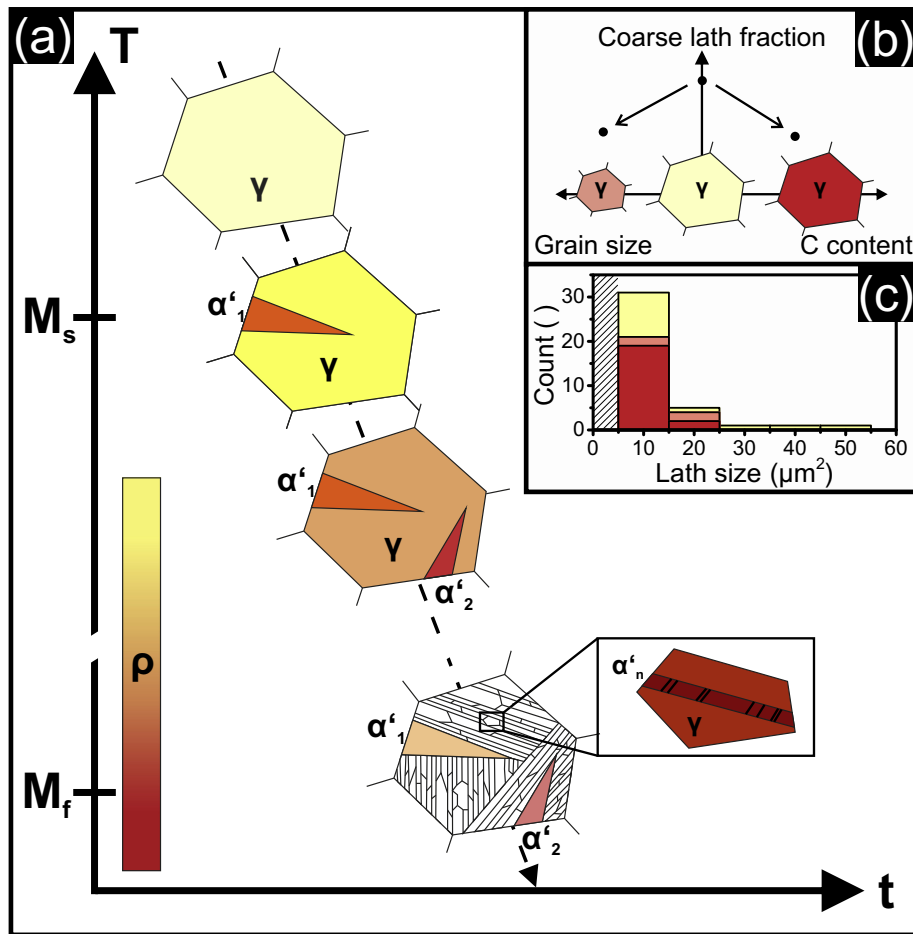


Fig. 7. (a) Schematic representation of the initial and final stages of martensitic transformation in one prior austenite grain along a model time-temperature curve with color-coded defect density (for simplicity an averaged defect density is shown in the austenite); Dependence of coarse lath area fraction on austenite grain size and C content shown schematically in (b) and by histogram analysis in (c) obtained by comparing a Fe-0.3C-5Ni alloy (dark red) and a 50 °C lower austenitized Fe-0.13C-5.1Ni alloy (light red) to the Fe-0.13C-5.1Ni base alloy (yellow). (For interpretation of the references to color in this figure legend, the reader is referred to the web version of this article.)

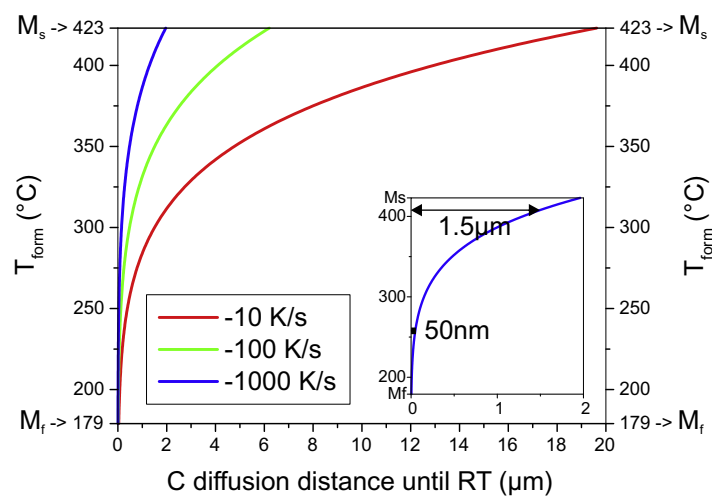


Fig. 8. C diffusion distance in martensite transformed at temperatures between Ms and Mf for -10, -100, -1000 K/s (magnified in the inset) linear cooling rates.

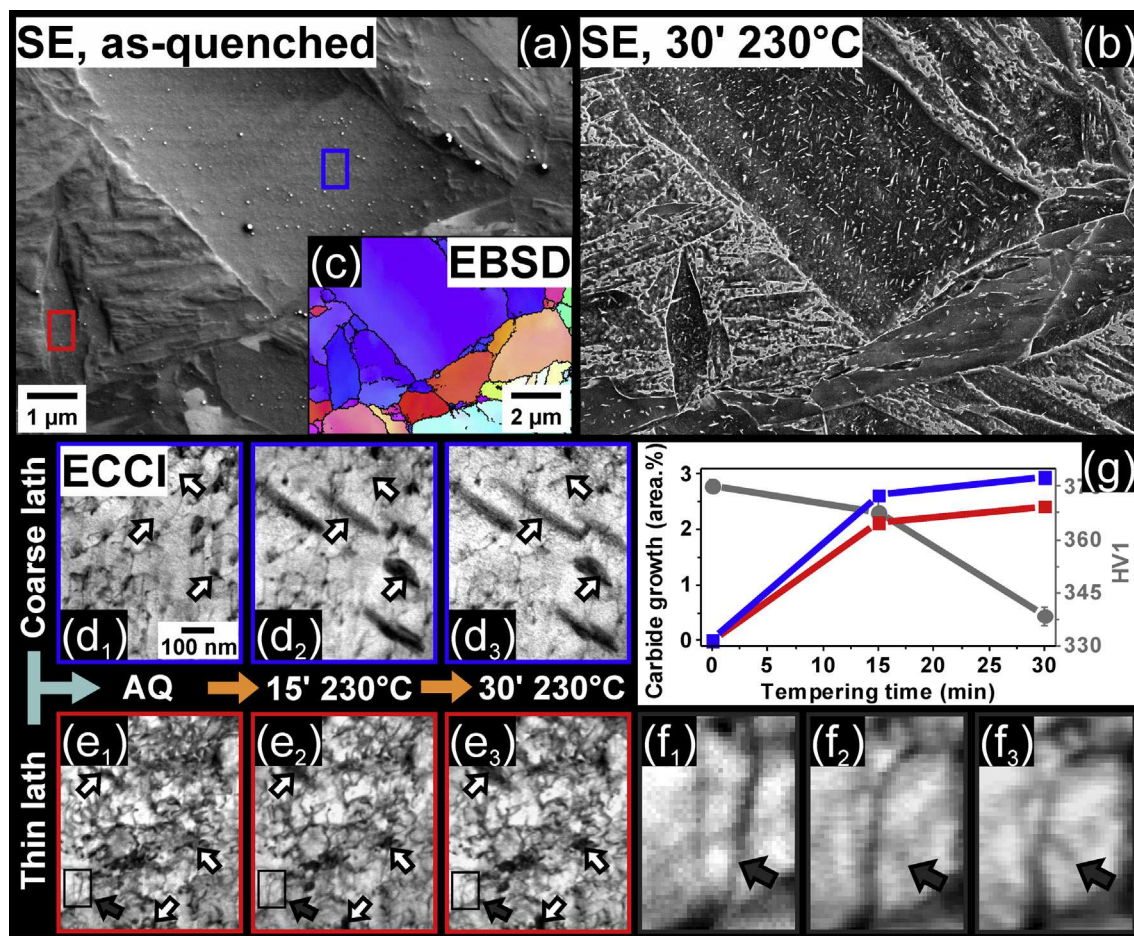


Fig. 9. Three-step quasi in-situ tempering from as-quenched condition shown in (a) to 30 min at 230 °C condition shown in (b); (c) IPF map of the analyzed region; defect structure and carbide precipitation tracked by ECCI during 15 min tempering steps for a coarse lath (d_1 – d_3) and a conventional thin lath region (e_1 – e_3). The nucleation and growth of carbides is indicated by arrows. ECCI reveals dislocation motions, e.g. in the thin lath (f_1 – f_3); (g) carbide growth and μ -hardness plotted against tempering time.

for higher C content) compared to the base alloy (8.8 area.%) investigated here. Fig. 7c shows the corresponding histogram analysis⁴ grouping the coarse laths by size for the three compared alloys. The count statistics are normalized by equal area measurements and show the limited occurrence of coarse laths when the initial austenite strength is increased.⁵ The M_s temperature decreases with decreasing austenite grain size or increasing C content [67,68]. Thus, both a finer austenite grain size as well as a higher C content harden the initial austenite structure compared to the coarse grained low C alloy (indicated by colored grain interior in Fig. 7b) and would lead to relatively smaller coarse laths due to the austenite's higher resistance against transformation.

In summary, there is now reasonable certainty about coupling the observed heterogeneity in lath size and defect structures to the intrinsic martensitic transformation sequence. Coarse laths, regardless of whether they transformed directly or developed through coalescence⁶, form early in the course of the martensitic

transformation. In the following sub-sections, we discuss the consequences of this process for C segregation and nanohardness.

4.2. Origin of carbon segregation heterogeneity

The results shown here confirm earlier observations that the thermally activated segregation of C atoms to lower energy positions in the microstructure can take place even during water quenching [23,39]. What is striking in the presented APT results shown here is that a significant heterogeneity exists within the microstructure in terms of the state of autotempering [23,39]. By site-specific APT analyses it is shown that the coarse lath regions are more autotempered with only ~0.15 at.% C remaining in the matrix. This matrix C concentration can be interpreted as the remaining C in interstitial positions. It has been shown that the largest fraction of the overall C is segregated to dislocations, but also to lath boundaries. These strong autotempering effects in the coarse laths also confirm their earlier transformation from the prior austenite (where C is homogeneously distributed), since the first transformed martensite dwells more time at higher temperatures compared to e.g. martensite that formed around M_f .

Fig. 8 shows the calculated diffusion distance of C atoms in the bcc-Fe matrix for transformation temperatures between M_s (~423 °C) and M_f (~179 °C) using the diffusion data in [23]. The curves correspond to –1000 K/s, –100 K/s and –10 K/s linear cooling rates. We find even for the fastest cooling rates that in the early transformed laths C can diffuse ~1.5 μ m until RT, while in the later

⁴ The histogram only shows the coarse lath fraction ($> 5 \mu\text{m}^2$), which is precisely captured by KAM mapping, while the size distribution of thin laths fails due to the EBSD resolution limits. Instead, an automated segmentation of ECC images resolving the thin lath structures is required, which is however currently not available.

⁵ It is obvious from the histogram analysis that a distribution of lath sizes exists in the microstructure ranging from the coarsest laths to the conventional thin lath matrix.

⁶ Further investigations are required through either in-situ cooling experiments [69] or phase field modeling [70] to confirm which process is more dominant. Interestingly, Spanos et al. [3] found different coarse martensite morphologies in the same microstructure hinting at both mechanisms occurring simultaneously.

transformed martensite C diffusion is almost frozen-in and confined to the nm-range (see the inset in Fig. 8). This also explains the presence of thin laths in the microstructure which are less autotempered compared to the coarse laths (see Fig. 5). It should be considered, however, that thin laths transform throughout the entire sequence of transformation except for the beginning, and thus they autotemper to different extents. The difference between early and late transformed thin laths is confirmed in the reconstructed APT sample in Fig. 5b.

Next we focus on the different morphology of C segregates. It is observed from APT analyses that C is segregated in the thin laths to 1D structures, while in the coarse lath regions to plate-like defects. While the former suggests dislocations, and the latter carbides (in agreement with Fonda et al. [4]), the associated C concentration in the C-rich plates (9.2 at.% C) is lower compared to cementite, ϵ - or other transition carbides. Thus, in order to confirm C segregation sites and processes, an interrupted low-T tempering experiment has been carried out where a polished and then quenched sample (Fig. 9a) is tempered in two steps of 15 min at 230 °C. The defect substructure (Fig. 9d₁–d₃) and carbide precipitation (Fig. 9e₁–e₃) of coarse laths (blue) and thin laths (red) were tracked by ECCI and quantified by image analysis (Fig. 9g). For representative statistics larger regions were analyzed (i.e. in Fig. 9 only some portions of the original ECCI images are shown). The experimental details are described elsewhere [71].

The heterogeneity in the carbide precipitation becomes obvious in the before-after overview images presented in Fig. 9a–b. The coarse lath has a high density of carbides⁷ compared to the surrounding thinner laths.⁸ Zooming in on the former, in the as-quenched condition small dark zones are observed (Fig. 9d₁) similar to those in the APT measurements (Fig. 5c). These zones develop with tempering to the typical plate-shaped carbides (Fig. 9d_{2–3}). This concludes that the plate-like features observed by APT are carbide nuclei or C clusters that form as a result of autotempering in the vicinity of C enrichment at dislocations. In the thin lath the precipitation of these zones can be also observed, however with smaller size and density (Fig. 9e₁). The higher rate of carbide growth is quantitatively shown in Fig. 9g. This can be explained to be due to the high degree of autotempering and lower dislocation density in the coarse laths, which leads to a stronger enrichment at the dislocations, from where carbides can easily nucleate.

In general, the number density of carbides is significantly lower than the dislocation density (see Fig. 9b). Thus, the sequence of C rearrangement and carbide growth requires thermal activation of most of the C trapped at dislocations to go back to solid solution, and then to transfer to form the carbide nuclei [72]. As soon as C is rejected from the majority of dislocations, a relaxation of the dislocation network is expected owing to the regained dislocation mobility. The quasi in-situ tempering experiment presented here captures an effect of this process: Fig. 9f₁–f₃ shows a magnified area of Fig. 9d₁–d₃, zooming in on few single dislocations. During the first tempering step (from Fig. 9f₁–f₂) a clear rearrangement of the dislocations is visible, whereas no changes are observed from the first to the second tempering step. Similar rearrangements are found in both, coarse and thin lath regions, but often only during the first tempering step, which suggests that they precede the initiation of the classical recovery process.

These confirmation experiments also enable reconsideration of the coalescence mechanism (see previous sub-section). For example, in coalesced bainite it was found that carbide precipitation is

localized in the center of the coalesced regions while there exists a precipitation-free zone at the periphery [57]. However, from Fig. 9b it is clear that this is not the case for coarse laths in our microstructure, where carbides are homogeneously distributed throughout the whole extended region. Contrary to coalesced bainite, in the case of lath martensite C might not diffuse at first preference toward the lath boundaries, but rather segregate to dislocations (see Fig. 5).

4.3. Origin of heterogeneity in local mechanical response

Expectedly, we observe a decrease in hardness with increasing tempering (Fig. 9g). This is in agreement with results from e.g. Ohmura et al. [73] who studied temper softening of Fe–C binary alloys. Here, we focus our discussion mainly on the effect of the transformation-induced microstructure heterogeneities in coarse and thin laths (lath size, defect density and C segregation) on the resulting heterogeneity of the mechanical response.

The presented analysis carefully takes into account the intrinsic statistical limitations of nanoindentation measurements, and reveals that the interior regions of the coarse laths are softer than the thin laths (Fig. 6d). This difference in nanohardness could be due to two effects: (i) difference in defect density and/or (ii) difference in C segregation. Hutchinson et al. suggested that the strength of lath martensite is not affected by C segregation when compared to C in solid solution [23]. This would require the observed nanohardness difference of ~ 0.5 GPa to be caused solely by different defect densities. However, the difference in dislocation densities (see Fig. 4) would account for a hardness difference of only ~ 0.01 GPa (calculated according to [23,74]), suggesting that the segregation of C still plays an influential role in the strength of martensite. The APT results revealed that in the thin laths a variety of autotempering states is reached where C is either still in solid solution (~ 0.7 at.%) or strongly segregated to dislocations (~ 8 at.%). In both cases a strengthening effect is expected, due to solid solution strengthening and dislocation pinning by C Cottrell atmospheres. However, in the coarse laths, which are most autotempered, C is found to be even stronger segregated, not only to dislocations, but more to plate-shaped defects (~ 9.2 at.%). In this case, C needs to dissolve from the dislocations in order to precipitate as C clusters and carbide nuclei. This partitioning mechanism reduces the C content in the matrix and hence decreases solid solution strengthening, i.e. only ~ 0.15 at.% C remains solved in interstitial positions. Also, it increases dislocation mobility since their C decoration has been reduced. These effects explain why the nanohardness of the coarse laths is decreased by about ~ 0.5 GPa in comparison with the thin laths that transform at lower temperatures. It should be noted though that these constituents with decreased hardness do not necessarily improve the toughness of martensitic steels. The toughness of both, bainitic and martensitic alloys are proposed to be deteriorated by the presence of coarse laths due to a lack of crack resistance sites in them enabling critical transgranular cracking [5]. In fact, we expect also an adverse effect due to the softness of coarse laths, making them less susceptible for crack propagation compared to the harder thin laths. The effect of the intrinsic lath size distribution on martensite microplasticity is clearly not fully understood so far and therefore subject of future investigations.

In summary, these micro-mechanical observations suggest that C solid solution strengthening as well as dislocation pinning are both important factors for the strength of martensite, and that lath martensite needs to be regarded as an “intrinsic” nano-composite structure as discussed by Allain et al. [75]. In the referred work, the characteristics of lath martensite stress–strain behavior were successfully modeled by applying a Continuum Composite Approach. In this model the microstructure of lath martensite is described

⁷ These carbides have three orientation variants which is in agreement with the literature [4].

⁸ For best comparison of carbide density, orientation effects in material removal during polishing and etching should be avoided. Thus, using the EBSD data (Fig. 9c) we concentrate on coarse and thin laths with a similar orientation marked in Fig. 9a.

as a mixture of soft and hard phases by implementing a stress spectrum corresponding to a local flow stress distribution in the microstructure. Our work provides the experimental evidence and explanation for the assumptions made by Allain et al. by revealing the corresponding microstructural heterogeneities in lath martensite.

5. Conclusions

To provide fundamental understanding of the micro-mechanical response of lath martensitic microstructures, a Fe–0.13C–5.1Ni alloy (wt.%) was investigated by 3D microstructure mapping coupled to high resolution ECCI, TEM nanodiffraction, APT and nanoindentation analyses. The following conclusions can be drawn:

- Lath martensitic microstructures are highly heterogeneous regarding the following aspects:
 - o *Size*: Lath martensitic microstructures are composed of “coarse laths” of various sizes embedded in a matrix of conventional thin laths. The coarse laths, which can be also observed in other martensitic steels reported in the literature, develop depending on the alloy C content and the prior austenite grain size.
 - o *Defect sub-structure*: The observed lath morphologies reveal significant differences in their defect sub-structure, e.g. for the Fe–0.13C–5.1Ni (wt.%) alloy investigated here, showing wide dislocation cell networks in the coarse lath regions and slightly higher dislocation densities in partially-twinned thin laths.
 - o *Composition*: Along with these morphological variations, a difference in the extent of autotempering is observed, e.g. in terms of C segregation. This extends on subsequent low temperature tempering to heterogeneous carbide precipitation in coarse and thin laths.
 - o *Mechanical response*: Consequently, the coarse lath regions represent “softer” zones in the microstructure and encourage us to interpret lath martensite as a nano-composite structure.
- These microstructural heterogeneities in lath martensite can be explained by the intrinsic course of martensitic transformation and the corresponding change of the austenite state (i.e. volume, defect density, compliance).
- For the systematic analysis of nanoscale phenomena in martensitic microstructures (e.g. C segregation), using high-resolution but low field-of-view techniques (e.g. atom probe tomography) requires careful consideration of the local heterogeneities arising from the martensitic transformation sequence, e.g. by employing the multi-probe approach presented here.
- From an alloy design perspective, control of the transformation sequence by adequately adjusting the thermomechanical treatment and the chemical composition could provide us new pathways to design lath martensitic microstructures with improved properties.

Acknowledgements

The authors gratefully acknowledge the funding by the European Research Council under the EU's 7th Framework Programme (FP7/2007–2013)/ERC Grant agreement 290998, and the funding by EU Research Fund for Coal & Steel (RFSR-CT-2013-00013) for the ToolMart project. We also want to thank David Barbier for supply of sample material and fruitful discussions, and our colleagues from the Max-Planck-Institut für Eisenforschung for their kind help.

Appendix A. Supplementary data

Supplementary data associated with this article can be found, in the online version, at <http://dx.doi.org/10.1016/j.actamat.2015.05.023>.

References

- [1] R.W. Fonda, G. Spanos, R.A. Vandermeer, *Scr. Metall. Mater.* 31 (1994) 683.
- [2] M. Katsumata, O. Ishiyama, T. Inoue, T. Tanaka, *Mater. Trans. JIM* 32 (1991) 715.
- [3] G. Spanos, R.W. Fonda, R.A. Vandermeer, A. Matuszeski, *Metall. Mater. Trans. A* 26 (1995) 3277.
- [4] R.W. Fonda, G. Spanos, *Metall. Mater. Trans. A* 45 (2014) 5982.
- [5] L.C. Chang, H.K.D.H. Bhadeshia, *Mater. Sci. Technol.* 12 (1996) 233.
- [6] G. Krauss, A.R. Marder, *Metall. Trans.* 2 (1971) 2343.
- [7] P.M. Kelly, J. Nutting, *Proc. R. Soc. Lond. Ser. A Math. Phys. Sci.* 259 (1960) 45.
- [8] S. Morito, H. Tanaka, R. Konishi, T. Furuhara, T. Maki, *Acta Mater.* 51 (2003) 1789.
- [9] S. Morito, X. Huang, T. Furuhara, T. Maki, N. Hansen, *Acta Mater.* 54 (2006) 5323.
- [10] H. Kitahara, R. Ueki, N. Tsuji, Y. Minamino, *Acta Mater.* 54 (2006) 1279.
- [11] C.C. Kinney, K.R. Pytlewski, A.G. Khachaturyan, J.W. Morris, *Acta Mater.* 69 (2014) 372.
- [12] E. Keehan, L. Karisson, H.K.D.H. Bhadeshia, M. Thuvander, *Mater. Charact.* 59 (2008) 877.
- [13] P. Hedström, A. Stormvinter, A. Borgenstam, A. Gholinia, B. Winiarski, P.J. Withers, O. Karlsson, J. Hagström, in: 1st International Conference on 3D Materials Science, TMS 2012, 2012, pp. 19.
- [14] D.J. Rowenhorst, A. Gupta, C.R. Feng, G. Spanos, *Scr. Mater.* 55 (2006) 11.
- [15] S. Morito, Y. Edamatsu, K. Ichinotani, T. Ohba, T. Hayashi, Y. Adachi, T. Furuhara, G. Miyamoto, N. Takayama, *J. Alloys Compd.* 577 (2013) S587.
- [16] C.A. Apple, R.N. Caron, G. Krauss, *Metall. Trans.* 5 (1974) 593.
- [17] A.R. Marder, G. Krauss, *Trans. ASM* 62 (1969) 957.
- [18] C. Zhu, A. Cerezo, G.D.W. Smith, *Ultramicroscopy* 109 (2009) 545.
- [19] C. Zhu, X.Y. Xiong, A. Cerezo, R. Hardwicke, G. Krauss, G.D.W. Smith, *Ultramicroscopy* 107 (2007) 808.
- [20] M.K. Miller, P.A. Beaven, S.S. Brenner, G.D.W. Smith, *Metall. Trans. A* 14 (1983) 1021.
- [21] K.A. Taylor, L. Chang, G.B. Olson, G.D.W. Smith, M. Cohen, J.B. Vandersande, *Metall. Trans. A* 20 (1989) 2717.
- [22] M.J. vanGenderen, S.J. Sijbrandij, A. Bottger, E.J. Mittemeijer, G.D.W. Smith, *Zeitschrift Fur Metallkunde* 88 (1997) 401.
- [23] B. Hutchinson, J. Hagström, O. Karlsson, D. Lindell, M. Tornberg, F. Lindberg, M. Thuvander, *Acta Mater.* 59 (2011) 5845.
- [24] Y. Toji, H. Matsuda, M. Herbig, P.-P. Choi, D. Raabe, *Acta Mater.* 65 (2014) 215.
- [25] L. Yuan, D. Ponge, J. Wittig, P. Choi, J.A. Jiménez, D. Raabe, *Acta Mater.* 60 (2012) 2790.
- [26] M.K. Miller, P.A. Beaven, G.D.W. Smith, *Metall. Trans. A* 12 (1981) 1197.
- [27] E.V. Pereloma, I.B. Timokhina, J.J. Jonas, M.K. Miller, *Acta Mater.* 54 (2006) 4539.
- [28] R.C. Thomson, M.K. Miller, *Scr. Metall. Mater.* 32 (1995) 149.
- [29] J. Wilde, A. Cerezo, G.D.W. Smith, *Scr. Mater.* 43 (2000) 39.
- [30] D. Raabe, S. Sandlöbes, J. Millan, D. Ponge, H. Assadi, M. Herbig, P.P. Choi, *Acta Mater.* 61 (2013) 6132.
- [31] D. Delagnes, F. Pettinari-Sturm, M.H. Mathon, R. Danoix, F. Danoix, C. Bellot, P. Lamesle, A. Grelrier, *Acta Mater.* 60 (2012) 5877.
- [32] R.C. Thomson, M.K. Miller, *Acta Mater.* 46 (1998) 2203.
- [33] S. Morito, K. Oh-ishi, K. Hono, T. Ohba, *ISIJ Int.* 51 (2011) 1200.
- [34] D.H. Sherman, S.M. Cross, S. Kim, F. Grandjean, G.J. Long, M.K. Miller, *Metall. Mater. Trans. A* 38 (2007) 1698.
- [35] G. Krauss, *Mater. Sci. Eng. A Struct.* 273 (1999) 40.
- [36] G.R. Speich, H. Warlimont, *J. Iron Steel Inst.* (1967) 385.
- [37] J.M. Chilton, P.M. Kelly, *Acta Metall.* 16 (1968) 637.
- [38] M. Kehoe, P.M. Kelly, *Scr. Metall.* 4 (1970) 473.
- [39] C. Lerchbacher, S. Zinner, H. Leitner, *Micron* 43 (2012) 818.
- [40] M. Herbig, D. Raabe, Y.J. Li, P. Choi, S. Zaefferer, S. Goto, *Phys. Rev. Lett.* 112 (2014) 126103.
- [41] R.K. Marceau, I. Gutierrez-Urrutia, M. Herbig, K.L. Moore, S. Lozano-Perez, D. Raabe, *Microscopy and Microanalysis: the Official Journal of Microscopy Society of America, Microbeam Analysis Society, 19, Microscopical Society of Canada*, 2013. 1581.
- [42] T. Swarr, G. Krauss, *Metall. Trans. A* 7A (1976) 41.
- [43] Y. Mine, K. Hirashita, H. Takashima, M. Matsuda, K. Takashima, *Mater. Sci. Eng. A* 560 (2013) 535.
- [44] H. Ghassemi-Armaki, P. Chen, S. Bhat, S. Sadagopan, S. Kumar, A. Bower, *Acta Mater.* 61 (2013) 3640.
- [45] A. Shibata, T. Nagoshi, M. Sone, S. Morito, Y. Higo, *Mater. Sci. Eng. A* 527 (2010) 7538.
- [46] S. Zaefferer, N.-N. Elhami, *Acta Mater.* 75 (2014) 20.
- [47] I. Gutierrez-Urrutia, S. Zaefferer, D. Raabe, *JOM* 65 (2013) 1229.
- [48] I. Gutierrez-Urrutia, S. Zaefferer, D. Raabe, *Mater. Sci. Eng. A Struct.* 527 (2010) 3552.
- [49] I. Gutierrez-Urrutia, D. Raabe, *Acta Mater.* 59 (2011) 6449.

- [50] I. Gutierrez-Urrutia, S. Zaefferer, D. Raabe, *Scr. Mater.* 61 (2009) 737.
- [51] T. Ohmura, K. Tsuzaki, S. Matsuoka, *Scr. Mater.* 45 (2001) 889.
- [52] T. Ohmura, T. Hara, K. Tsuzaki, *J. Mater. Res.* 18 (2003) 1465.
- [53] D. Kiener, C. Motz, M. Rester, M. Jenko, G. Dehm, *Mater. Sci. Eng. A Struct.* 459 (2007) 262.
- [54] C. Cayron, *J. Appl. Crystallogr.* 40 (2007) 1183.
- [55] Y.J. Li, P. Choi, C. Borchers, S. Westerkamp, S. Goto, D. Raabe, R. Kirchheim, *Acta Mater.* 59 (2011) 3965.
- [56] I. Gutierrez-Urrutia, D. Raabe, *Scr. Mater.* 66 (2012) 343.
- [57] H.K.D.H. Bhadeshia, E. Keehan, L. Karlsson, H.O. Andren, *Trans. Indian Inst. Met.* 59 (2006) 689.
- [58] H. Pous-Romero, H. Bhadeshia, *J. Press. Vessel Technol.* 136 (2014).
- [59] J.H. Pak, H.K.D.H. Bhadeshia, L. Karlsson, E. Keehan, *Sci. Technol. Weld. Join.* 13 (2008) 593.
- [60] G. Miyamoto, A. Shibata, T. Maki, T. Furuhashi, *Acta Mater.* 57 (2009) 1120.
- [61] S.M.C. Van Bohemen, J. Sietsma, *Metall. Mater. Trans. A* 40 (2009) 1059.
- [62] Y. Matsuoka, T. Iwasaki, N. Nakada, T. Tsuchiyama, S. Takaki, *ISIJ Int.* 53 (2013) 1224.
- [63] E. Jimenez-Melero, N.H. van Dijk, L. Zhao, J. Sietsma, S.E. Offerman, J.P. Wright, S. van der Zwaag, *Scr. Mater.* 56 (2007) 421.
- [64] C.N. Hsiao, C.S. Chiou, J.R. Yang, *Mater. Chem. Phys.* 74 (2002) 134.
- [65] G.R. Speich, P.R. Swann, *J. Iron Steel Inst.* (1964) 480.
- [66] S. Kajiwar, *Metall. Trans. A* 17 (1986) 1693.
- [67] H. Yang, H. Bhadeshia, *Scr. Mater.* 60 (2009) 493.
- [68] K. Ishida, *J. Alloys Compd.* 220 (1995) 126.
- [69] S. Nambu, N. Shibata, M. Ojima, J. Inoue, T. Koseki, H.K.D.H. Bhadeshia, *Acta Mater.* 61 (2013) 4831.
- [70] H.K. Yeddu, A. Malik, J. Ågren, G. Amberg, A. Borgenstam, *Acta Mater.* 60 (2012) 1538.
- [71] J.-L. Zhang, L. Morsdorf, C.C. Tasan, D. Raabe, in preparation.
- [72] G.R. Speich, W.C. Leslie, *Metall. Trans.* 3 (1972) 1043.
- [73] T. Ohmura, T. Hara, K. Tsuzaki, *Scr. Mater.* 49 (2003) 1157.
- [74] P.M. Rice, R.E. Stoller, *Fundamentals of Nanoindentation and Nanotribology II. Symposium, 2001*, pp. Q7.11.1–Q7.11.6.
- [75] S. Allain, O. Bouaziz, M. Takahashi, *ISIJ Int.* 52 (2012) 717.